Geophysical Research Letters

RESEARCH LETTER
10.1029/2021GL094174

Key Points:

- A $M_w = 8.5$ event in central Cascadia (Oregon) can create coastal tsunami amplitudes comparable to those from the largest possible event
- The concave coastline contributes to larger coastal tsunami amplitudes in central Cascadia
- The choice of slip model does not significantly affect the distribution of coastal tsunami amplitudes in Cascadia

Supporting Information:

Supporting Information may be found in the online version of this article.

Correspondence to:

A. Salaree,
salaree@umich.edu

Citation:

Salaree, A., Huang, Y., Ramos, M. D., & Stein, S. (2021). Relative tsunami hazard from segments of Cascadia subduction zone for M_w 7.5–9.2 earthquakes. *Geophysical Research Letters*, *48*, e2021GL094174. https://doi.org/10.1029/2021GL094174

Received 14 JUN 2021
Accepted 30 JUL 2021

Relative Tsunami Hazard From Segments of Cascadia Subduction Zone For M_w 7.5–9.2 Earthquakes

Amir Salaree[1], Yihe Huang[1], Marlon D. Ramos[1,2], and Seth Stein[3]

[1]Department of Earth and Environmental Sciences, University of Michigan, Ann Arbor, MI, USA, [2]U.S. Air Force Research Laboratory, Albuquerque, NM, USA, [3]Department of Earth and Planetary Sciences and Institute for Policy Research, Northwestern University, Evanston, IL, USA

Abstract Tsunamis from earthquakes of various magnitudes have affected Cascadia in the past. Simulations of M_w 7.5–9.2 earthquake constrained by earthquake rupture physics and geodetic locking models show that $M_w \geq 8.5$ events initiating in the middle segments of the subduction zone can create coastal tsunami amplitudes comparable to those from the largest expected event. Our rupture and tsunami simulations reveal that the concave coastline geometry of the Pacific Northwest coastline focuses tsunami energy between latitudes 44° and 45° in Oregon. The possible coastal tsunami amplitudes are largely insensitive to the choice of slip model for a given magnitude. These results are useful for identifying the most hazardous segments of the subduction zone and demonstrate that a worst-case rupture scenario does not uniquely yield the worst-case tsunami scenario at a given location.

Plain Language Summary Offshore earthquakes along the Pacific Northwest coast of the U.S. and Canada (Cascadia region) can have magnitudes as high as 9.2, as was probably the case for an earthquake in the year 1700 CE that resulted in a large tsunami in Cascadia and across the Pacific Ocean. To learn more about the future tsunami hazard in the region, we design computer models of tsunamis from a wide range of earthquake scenarios. We find that almost regardless of the earthquake source details, events larger than magnitude 8.5 near the coast of Oregon can create large and widespread tsunamis along the US west coast. These are consequences of the geometry of offshore earthquake faulting and the concave shape of coastline in the region.

1. Introduction

Coupling between the subducting Juan de Fuca plate and the overriding North America at the shallow-dipping Cascadia subduction zone (Crosson & Owens, 1987) is expected to cause future large earthquakes and tsunamis. Previous studies (Atwater, 1987; Goldfinger et al., 2017; Satake et al., 2003) show that the ~1,100 km plate boundary extending from British Columbia to northern California has generated large tsunamis in the past. The tsunami from the most recent great Cascadia earthquake or sequence of events, with an inferred total magnitude of 9 (Melgar, 2021), devastated the American and Japanese coasts on January 26, 1700 (Satake et al., 1996) as shown by Native American oral traditions (Heaton & Snavely, 1985) and detailed Japanese written accounts (Atwater et al., 2015). Geological and paleoseismic evidence also indicates earlier prehistoric tsunamigenic events (Atwater et al., 1991; Darienzo & Peterson, 1995; Goldfinger et al., 2012; Peters et al., 2003).

A major challenge to modeling future Cascadia tsunami hazards is the large uncertainty in recurrence interval. Very large Cascadia events seem to occur on average every 400–500 years, and smaller events ($M_w \lesssim 8.7$) are thought to occur every ~200 years. However, the uncertainties in these measurements are sometimes on the same order of magnitude as the measurements themselves (e.g., Goldfinger et al., 2012; Kelsey et al., 2005). Hence, it is challenging to assess tsunami hazards from different rupture segments along the coast (e.g., González et al., 2009). Along-strike segmentation in the subduction zone is usually associated with variabilities in outer wedge morphology and structure (Watt & Brothers, 2021). Another source of uncertainty is the limited constraints on the location and size of slipping segments of the subduction zone, and thus the magnitude of future earthquakes, due to the absence of well-constrained information on the lateral extent of past ruptures (e.g., Goldfinger et al., 2017; Witter et al., 2011).

Tsunami hazard in Cascadia has been modeled as a function of various recurrence intervals and earthquake magnitudes, yielding results expressed as hazard curves and inundation maps for sites along the coast (e.g., Park et al., 2017; Priest et al., 2013; Thio & Somerville, 2009; Thio et al., 2010). Such studies, which are also conducted for other, better-documented subduction zones (e.g., Satake, 2015) are useful in planning response to tsunamis (Lindell & Prater, 2010). However, they often do not distinguish between hazards due to rupture from various sections of the subduction zone.

Our study aims to identify the most hazardous segments of the Cascadia subduction zone by considering a range of earthquake scenarios and resulting tsunamis. In this regard and to estimate the maximum expected tsunami amplitudes for Cascadia earthquakes, we use a set of rupture scenarios derived by scaling the slip distribution prescribed by geodetic locking models as initial conditions for tsunamis. We then compare our tsunami simulation results to those based on dynamic ruptures as well as perturbed versions of these rupture scenarios to identify the contribution of various portions of the subduction zone. Finally, we use simple numerical experiments with synthetic bathymetry to investigate the contribution of Cascadia coastal morphology to the distribution of tsunami amplitudes. The result helps us better understand the contribution of source and coastal components to Cascadia tsunamis.

2. Methods

2.1. Rupture Model & Scaling of Slip

Our earthquake simulations are based on locking models that estimate the slip deficit on the plate interface needed to match geodetic observations (Priest et al., 2010; Schmalzle et al., 2014; Li et al., 2018; Small & Melgar, 2020). If all the deficit were released in a single earthquake, the model would yield the maximum possible slip and the largest earthquake. However, the next event may not release all the accumulated stress. To achieve the largest tsunami amplitudes, we use the Gamma locking model from Schmalzle et al. (2014). This model represents high levels of slip-deficit extending to the trench (Figure 1d). In contrast with rupture scenarios with more uniform slip distributions, releasing the accumulated slip mostly confined near the trench would result in pulse-like, relatively short-period tsunami fronts. Due to very large seafloor uplift in the immediate vicinity of the trench, such a rupture scenario results in relatively larger coastal tsunami waves, especially in the near-field. By assuming an average recurrence interval T_r for stress release, as inferred from offshore turbidite deposits (Goldfinger et al., 2012, 2017), we convert the slip rate deficit in the locking model to slip. An average value of T_r, that is 320 years (Goldfinger et al., 2017) results in a maximum slip amplitude of ~20 m along the trench in northern Cascadia.

In order to investigate the largest tsunamis, we discretize the rupture into 25 × 25 km blocks (Figure 1) to satisfy numerical hydrodynamic sufficiency threshold (see Section 2.2), each of which is considered as a pure double-couple source with the dip of the slab, the azimuth of the trench, and a slip angle of 90°. We then calculate a surface deformation field (Mansinha & Smylie, 1971) using the average slip value within the block. Because smaller earthquakes require less accumulated stress over shorter recurrence time, they result in smaller fault slip. We estimate the slip for smaller earthquakes and produce their seafloor deformation fields by scaling down the deformation field for the largest event (Figure 1) using earthquake scaling laws (Geller, 1976) that have been used in past tsunami studies (e.g., Okal, 1988). The scaling scheme used to estimate slip based on seismic moment for smaller earthquakes can significantly affect the calculated tsunami amplitudes. For instance, Thingbaijam et al.'s (2017) scaling equations result in tsunami amplitudes up to five times smaller due to the underestimation of slip by the scaling law we used (Figure S1). However, the main trends of coastal amplitude distribution are not affected by the choice of scaling equations (see Supporting Information).

We construct a field of ocean floor dislocations for six magnitudes: M_w = 7.5, 8.0, 8.5, 9.0, 9.1, and 9.2 (Figure 1). The two largest magnitudes are selected to obtain better resolution of the tsunami hazard for the potentially largest events. The hypocenter is not positioned at the trench to guarantee that the rupture nucleates between the surface and the base of the seismogenic zone near ~30 km depth (Wang & Tréhu, 2016). For each magnitude we start rupture scenarios at the northernmost block for the chosen geometry and propagate the rupture southward until it is large enough to yield the desired magnitude. Rupture propagates along strike and dip with speeds between 2 and 3 km/s before reaching the bottom of the seismogenic zone,

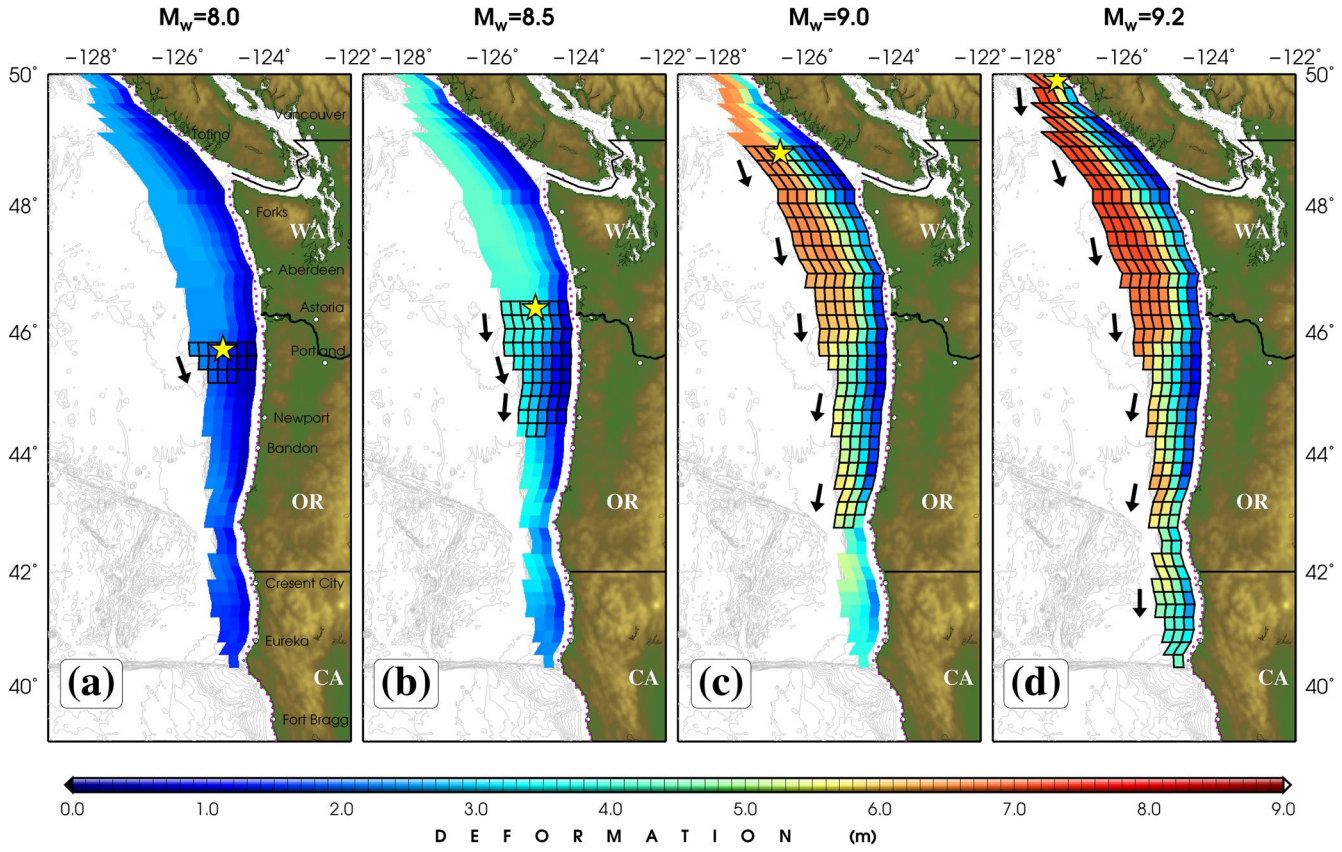

Figure 1. Scaled dislocation fields at the ocean floor calculated from the locking model for (a) $M_w = 8.0$, (b) $M_w = 8.5$, (c) $M_w = 9.0$, and (d) $M_w = 9.2$. Meshes show sample north-south rupture scenarios s. Black arrows denote the direction of rupture propagation from the hypocenters marked by yellow stars.

mimicking an elliptical rupture. This process is then repeated by moving the hypocenter one block south, resulting in a new rupture scenario with the entire rupture region moved south. This approach leads to 118 rupture scenarios. In our model, ruptures of $M > 8.5$ earthquakes primarily propagate along strike because the down-dip rupture extent saturates, resulting in an elongated rupture area (Figure 1). This process yields a frequency-magnitude distribution similar to the Gutenberg-Richter distribution due to the constraints resulting from rupture areas on the overall seismic moment (Stein & Wysession, 2009; Figure S2). Our arbitrary choice of rupture directivity (north to south) has little effect because the proximity of the coastlines to the trench (~150 km) and the large dominant wavelength of the tsunami (Rabinovich, 1997) prevent the rupture duration from significantly affecting the coastal tsunami amplitudes. Numerical experiments with various modes of rupture in flat oceans and near coastlines of different morphologies reveal that the contribution of rupture directivity is not significant in the near field (Figure S3), as also shown by Williamson et al. (2019). One can show that (see Supporting Information) in the absence of small-scale disturbances at narrow openings, the internal structure of ruptures in deep oceans is practically not transferred into shallow basins. The virtual gauge at the shallow entrance of Salish Sea (marked by red circles in across Figure 2) records no sign of nonlinear behavior throughout our simulations (tsunami amplitudes decay as predicted by Green's law [Green, 1838]). Thus, we do not anticipate the kinematics of Cascadia ruptures to affect the tsunami waves at Seattle.

2.2. Tsunami Simulation Method

We simulate tsunamis from each scenario using the MOST algorithm (Titov et al., 2016) that solves the fully nonlinear version of the shallow water approximation of the Navier-Stokes equation. MOST has been extensively validated through comparisons with laboratory and field data using standard international protocols (Synolakis et al., 2008). Simulations are performed for 4.5 h time windows, allowing the tsunami to

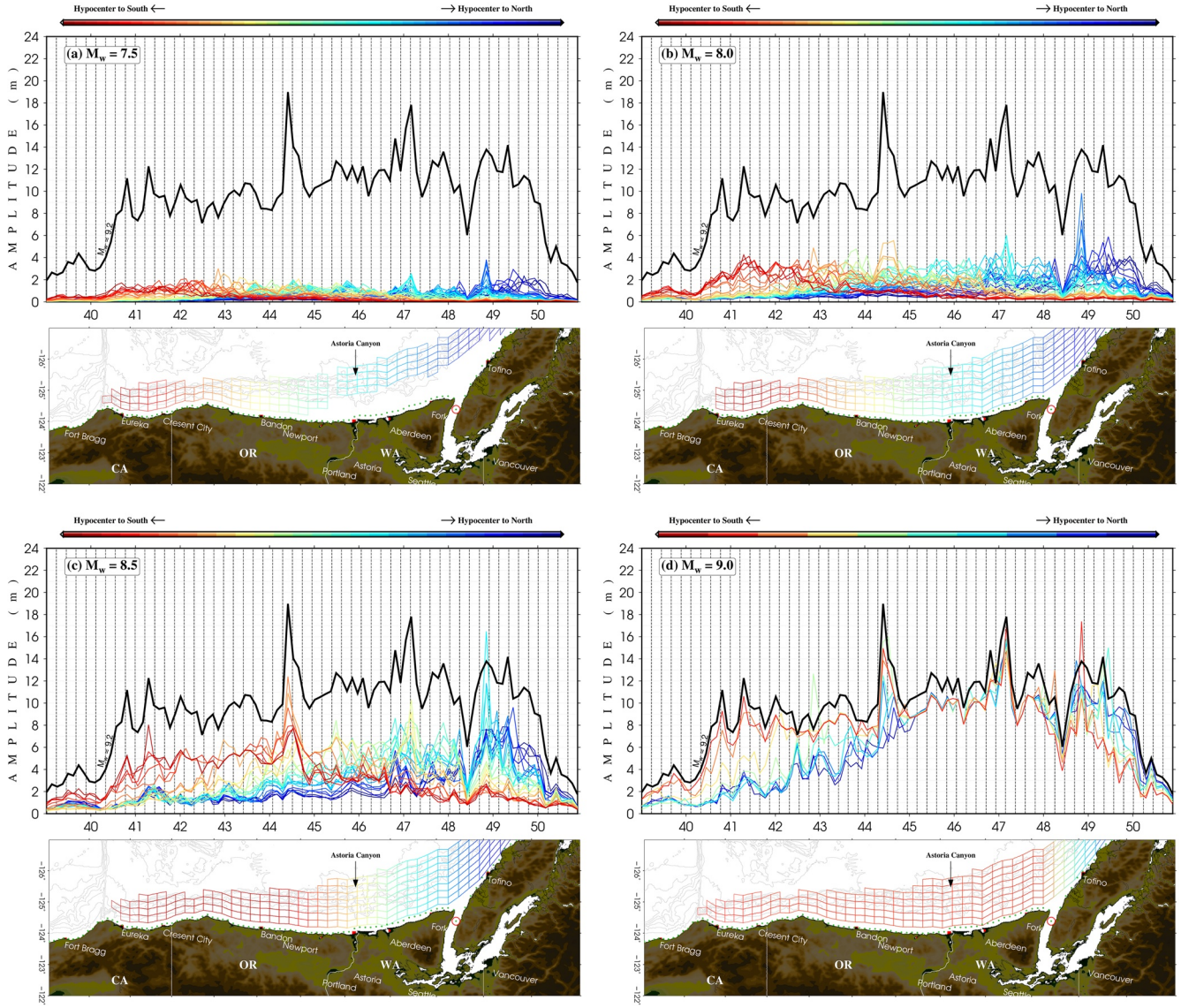

Figure 2. Distribution of coastal tsunami amplitudes across latitude for (a) $M_w = 7.5$, (b) $M_w = 8.0$, (c) $M_w = 8.5$, and (d) $M_w = 9.0$ ruptures. (top) The curves are color-coded according to hypocenter latitude with hot colors in the south and cold colors in the north. Black curve shows coastal tsunami amplitudes for the $M_w = 9.2$ event; (bottom) Cascadia coastline and the rupture blocks are colored to provide a sense of hypocenter latitude. Gray contours indicate bathymetry. Large population centers are shown for reference. The red circle denotes the single virtual gauge at the entrance of Salish Sea.

propagate along the entire coast. These simulations use 0.5 s time steps to satisfy the stability-resolution requirement (Courant et al., 1928). Wave height calculations are truncated at a depth of 30 m along the coastlines (typically at a distance of 1–4 km) to avoid nonlinear shoaling effects, especially in the presence of large offshore deformation values. Therefore, no run-up values are calculated. Although run-up typically increases the tsunami hazard for generally linear coastal bathymetry, in the absence of bays, the distribution of coastal amplitudes (at shallow depth) will almost match that of run-up (Plafker, 1997). We calculate time histories of tsunami amplitudes at 100 virtual gauges along the coastline at a depth of ~35 m and one gauge at the entrance of the Strait of Juan de Fuca, north of Fork. We use GEBCO bathymetry interpolated to a spatial resolution of 18 arc-seconds to ensure enough (~20) grid points per wavelength (Shuto et al., 1986).

MOST was developed to model static sources and cannot be directly applied to kinematic ruptures (Titov & Synolakis, 1998). Hence, we apply it to the discretized rupture blocks each of which happens at time t_i after the origin time. For each block, calculations are terminated after a duration Δt_i and the outputs are

fed into MOST as initial conditions for the next block. The process continues until rupture ends after which the problem turns into a regular tsunami propagation. Although this approach introduces discontinuities in both water surface elevation and velocity, it produces results comparable to those from fully kinematic algorithms such as GeoClaw (Berger et al., 2011; González et al., 2011) that have been verified for Cascadia (Melgar et al., 2016). The discrepancy between our results and those from the previous studies is largely due to the scaling equations. As discussed earlier (Figure S1) Geller's (1976) scaling equations predict larger slip for a given rupture. While kinematic rupture properties do not significantly affect near-field tsunami propagation, we consider kinematic ruptures for a more comprehensive view of tsunami behaviors.

3. Cascadia Earthquake and Tsunami Scenarios

3.1. Tsunami Simulation Results

We analyze the tsunami hazard for our rupture scenarios (Figure 1) by simulating the resulting tsunamis. Our magnitude range of $M_w = 7.5$–9.2 accommodates both the largest expected rupture and the smallest rupture with noticeable ocean floor deformation (~1 m). Note that the smallest rupture does not necessarily reach the ocean floor. Tsunami simulations for the rupture scenarios are shown in Figure 2 (also see Supporting Information). We find that various earthquake magnitudes can create similar tsunami amplitudes at a given location depending on the position of the hypocenter. For example, as shown in Figures 2c and 2d, a $M_w = 8.5$ earthquake with a hypocenter in the south (~43°N) and a $M_w = 9.0$ earthquake starting further north (~48°N) both produce tsunami amplitudes of ~8 m at Newport (~44.5°N). This partly reflects geometrical spreading wherein the energy flux in the propagating tsunami decreases with increasing distance. However, as seen in Figure 2, this trend is not monotonic.

Spatial variation of near-shore tsunami amplitudes from large sources mostly reflects the influence of piecewise coastal slopes (Kânoğlu & Synolakis, 1998), because the near-shore bathymetry of Cascadia varies little with latitude (with the exception of the Astoria Canyon (Griggs & Kulm, 1970)). In fact, bathymetric profiles across all latitudes within 400 km from shoreline have a correlation coefficient (CC) of ≈0.75. Hence, in the absence of major bathymetric features the largest amplitudes occur at the latitudes with the largest earthquake slip (e.g., near Washington), due to geometrical spreading and directivity (Aki & Richards, 2002; Ben-Menahem & Rosenman, 1972). The latter causes the waves to interfere constructively in a direction perpendicular to the rupture, focusing tsunami energy onto the closest shorelines. This effect can be readily seen in the cumulative field of maximum tsunami amplitudes; Figure 3 shows the sum of maximum tsunami amplitudes across all scenarios for each magnitude.

The simulations reveal that in the absence of significant local bathymetric features, the concave geometry of the coast between 43° and 48°N concentrates amplitudes in central Cascadia (between 44° and 45°N; around Newport, Oregon) especially from ruptures in central Cascadia, in agreement with edge wave theory (Munk et al., 1956). We carried out numerical tsunami simulations in flat oceans along narrow, shallow continental shelves to study the effects of a coastline curvature (Figures 3e and 3f) on tsunami amplitudes. These experiments show that coastline concavity increases the tsunami energy in the nadir (here, mid-latitudes) by focusing the energy of edge wave modes along the coast, on the continental shelf (the peak in vertical bars in Figure 3f). Another amplitude peak offshore, which approaches the shoreline by increasing curvature, results from the concentration of tsunami reflection at the focal point of the curved shoreline (marked by a yellow star in Figure 3e). The cluster appears at half the radius of coastline curvature (i.e., focal point) of coastline analogous to that predicted by geometric optics for concave mirrors. While in Cascadia the latter cluster would appear at a long distance (~500 km) from the shoreline and thus does not contribute to coastal amplitudes, the former increases the amplitudes at ~44°N as shown in Figures 3a–3d. Our numerical simulations show that the increase in radius of coastal curvature determines the extent and size of both peaks (for more discussion see Figure S4, and the Movie S1).

Given the shoreline's large radius of curvature (~1,000 km), the latter cluster would appear at a long distance (~500 km) from the shoreline and thus does not contribute to coastal amplitudes, the former increases the amplitudes at ~44°N by about 10% (Figures 3a–3d). We attribute the relatively larger amplitudes near Oregon in all the scenarios (Figure 2) to this phenomenon. Although this effect makes Oregon coast almost as hazardous as northern regions (near Washington), it does not violate the generalizations that

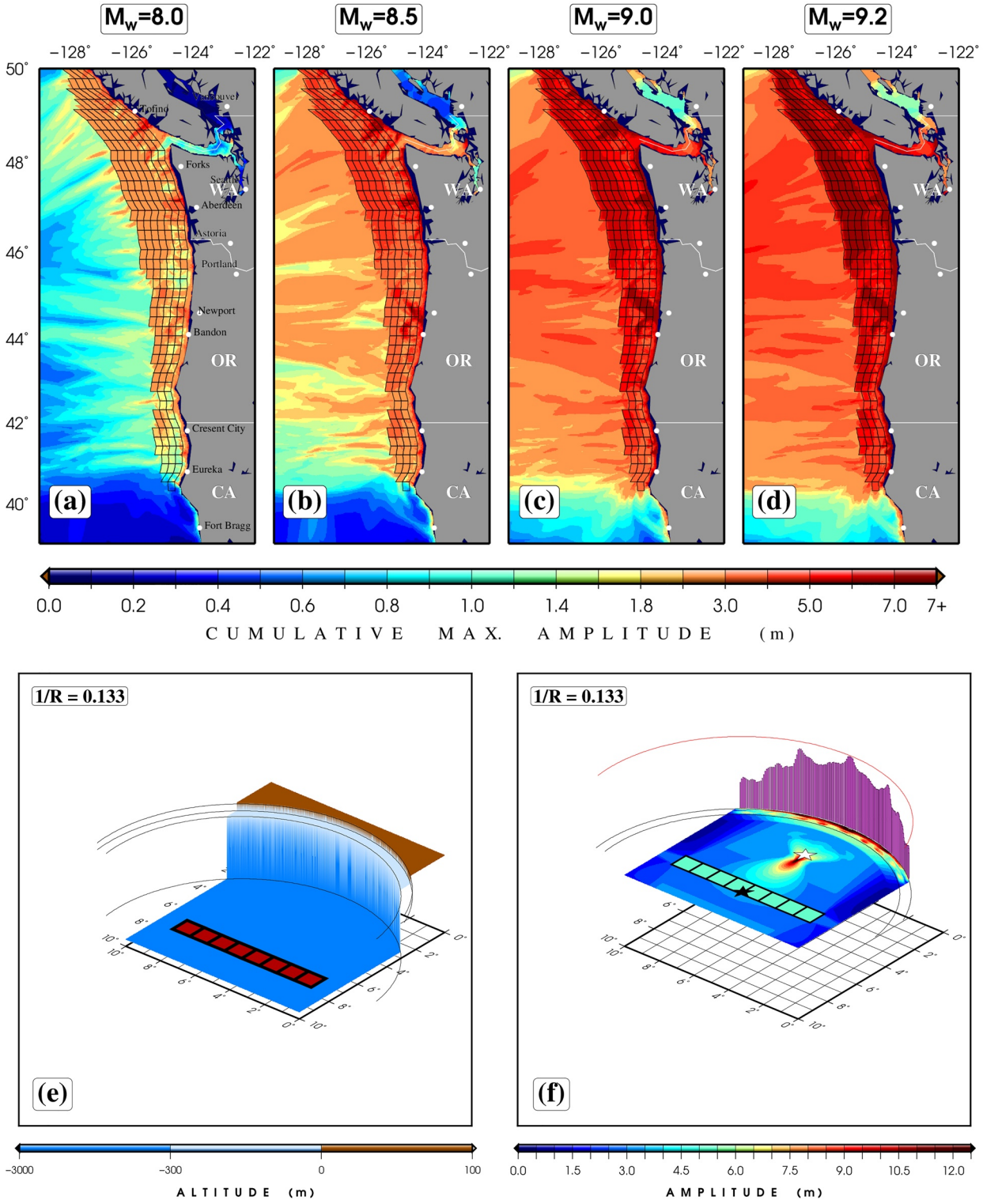

Figure 3. Cumulative maximum tsunami amplitudes for (a) $M_w = 8.0$, (b) $M_w = 8.5$, (c) $M_w = 9.0$, and (d) $M_w = 9.2$ source scenarios. Each panel shows the largest tsunami amplitudes across all rupture scenarios for a given magnitude. (e) An example of synthetic bathymetry (flat ocean with a curved, narrow continental shelf and a coastline) used to study the effects of curvature. The red array of "blocks" depicts the static rupture. (f) Maximum tsunami amplitudes for the scenario in (e). Vertical pink bars represent maximum coastal tsunami amplitudes. Black and yellow stars show the center of curvature and focal point of the curved coastline, respectively.

smaller earthquakes create smaller tsunamis, and that shorelines closer to large fault slip experience larger tsunami waves, which are generally true for linear coastlines and in the absence of bays (Davies et al., 2018) (Figures S3–S5).

Another interesting simulation result is the apparent relative immunity of a portion of northern California coastlines south of Cape Mendocino to Cascadia tsunamis, especially from $M_w < 9.0$ earthquakes with hypocenters in the north. At first glance, this is surprising given the region's proximity to a slip cluster near the southern tip of the rupture. However, it results from both the end of rupture and the convex promontory near Eureka (Figure 2), south of where coastal amplitudes drop. Simulations suggest that the coastal morphology creates and scatters free edge waves (supporting information), making the California shorelines virtually sheltered.

The secondary large peaks in Figure 2 can be attributed to either local, small-scale bathymetric features or the secondary edge wave modes (also seen in Figure 3f). The actual character of such locally large amplitudes is difficult to resolve due to the nonlinear interaction of hydrodynamic modes. Another noteworthy feature across Figure 2 is the locally large amplitudes at ~49°N appearing for only the ruptures initiating at that latitude (note that ruptures with hypocenters at larger latitudes do not create this feature). This feature is possibly due to instabilities in the numerical solutions of the kinematic problem at block edges arising from the scheme used in the hydrodynamic algorithm (Titov & Synolakis, 1998). This would explain the absence of these amplitudes in the $M_w = 9.2$ scenario which span the entire plate interface.

3.2. Choice of Slip Model

The distribution of potential slip from the locking model shows two main clusters (Figure 1d). The larger cluster (both in area and slip magnitude) is in the north, close to British Columbia, and the smaller one is around 44°N. However, the tsunami simulation results are not significantly affected by the choice of slip models on a regional scale. We simulate tsunamis using a simple slip model (modified from Priest et al., 2010) and found similar results to those from our more physical model. As shown in Figures 4a–4e, the coastal amplitudes show a CC of 0.8. We also used a dynamic rupture model with identical recurrence intervals, derived from a Gaussian locking model (Ramos et al., 2021; Schmalzle et al., 2014). Such models consider the dynamic interaction of fault stresses and frictional strengths, and near-trench slip can be amplified due to constructively interfering free-surface reflections within the accretionary wedge. The resulting tsunami simulations yield a similar (CC = 0.8) distribution of coastal amplitudes (Figure 4j).

The absolute values of coastal tsunami amplitudes from these simpler models can locally vary from our modeling results by up to 30%. However, the general trend of tsunami amplitudes remains similar. In the absence of conclusive geodetic and seismic constraints on fault locking, we think our model adequately represents potential future ruptures and consider the 30% discrepancy as illustrating the uncertainty.

Simulation of the tsunami from a perturbed version of our choice of locking model (created by introducing white noise equal to 50% of the maximum to the deformation field of the parent model) yields a significantly different distribution (CC = 0.3) of coastal tsunami amplitudes (Figure S6). We attribute this discrepancy to the disruption of large-scale slip clusters which changes the dominant period of the tsunami. Such smaller wavelengths significantly alter the interaction of the tsunami with the shoreline, thus resulting in a different pattern of coastal amplitudes. Otherwise, given the similar bathymetry along strike, different rupture models with comparable dimensions of slip clusters (bearing an absence of large slip deficit in central Cascadia; Li et al., 2018) would result in similar tsunamis.

4. Discussion and Conclusions

Simulations of tsunamis from physics-based $M_w = 7.5$–9.2 earthquake rupture scenarios show that largest and most widespread coastal tsunami amplitudes result from ruptures at or starting from mid-latitudes in central Cascadia. This result is almost independent of the choice of slip model as long as the dimensions of major slip clusters are preserved. Such ruptures, especially with $M_w > 8.5$, can create tsunami amplitudes exceeding 50% of those from the largest expected $M_w = 9.2$ rupture (Figure S7a). Statistical analysis using the metric MT (Salaree & Okal, 2020) suggests that the near-field propagation patterns of tsunamis from

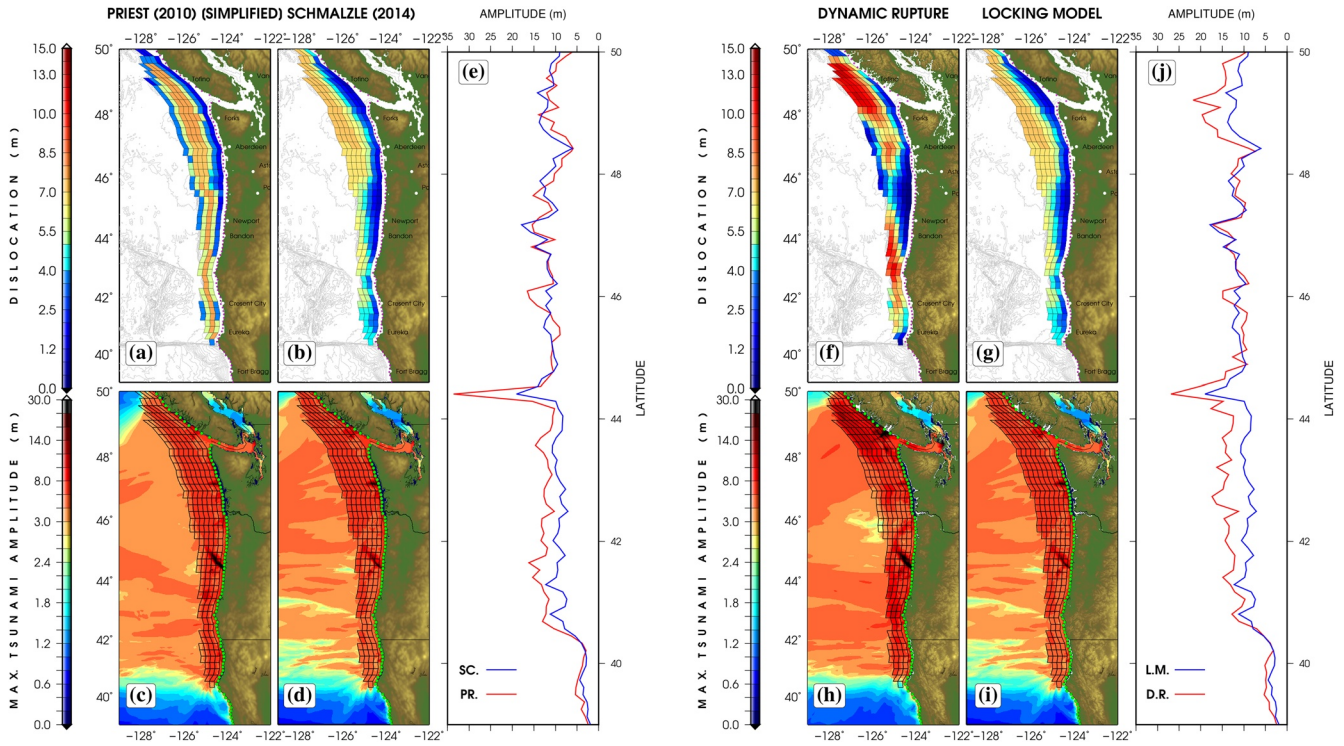

Figure 4. (a) A simplified locking model (Priest et al., 2010) produces similar tsunami amplitudes to those from our model shown in (b), both in the Pacific (c and d) and along the coastline (e). Also, a dynamic $M_w = 9.2$ rupture (Ramos et al., 2021) derived from the Gaussian locking model (f) and our choice of locking model (g) result in similar tsunami amplitudes both in the Pacific (h and i) and along the coastline (j). The dots next to coastline show locations of virtual gauges.

$M_w > 8.5$ events are very similar (Supporting Information). This effect is important because realistic estimates of the expected loss are valuable in designing mitigation policy (Stein & Stein, 2014). Although smaller earthquakes generate smaller tsunamis, their expected amplitudes (up to 12 m using our choice of scaling law) are significant. Thus, smaller earthquakes (M ~ 8–8.5) that are more likely to occur in the near future may create comparable—though more localized—damage than the less frequent worst-case scenario (e.g., Priest et al., 2010; Thio et al., 2010). An important point to note is that in our algorithm of rupture design individual rupture segments with identical slip are included in several simulations in order to investigate the effect of rupture location and size. However, the shape of slip model does change from a more or less circular rupture (similar rupture length and width) for smaller ($M < 8.5$) ruptures to more elongated, larger ruptures (Figure 1). This is consistent with our understanding of earthquake source physics.

We also find that the large-scale morphology of Cascadia's coastline focuses and defocuses tsunami energy. Simulations (Figure S4 and Movie S1) show that coastline curvature can increase the coastal tsunami amplitude by more than 10%. Comparison of Cascadia with other subduction zones where coastal curvature is insignificant (i.e., Chile with curvature of ~0.017) shows why such heightened tsunami amplitudes are not observed in these regions. Our simulations show that the southernmost sites (Fort Bragg, Eureka, and Crescent City, Figures 2 and 3) show almost no change in the tsunami amplitudes for events with increasing magnitude above $M_w = 9.0$ (Figure 2), due to the large promontory at ~42.5°N separating the concave coastline from that to the south (Figure S5a). Examination of the along-strike tsunami amplitudes (Figure 3) reveals that the relative differences throughout the simulation area are small (sometimes <1 m) for earthquakes larger than $M_w = 9.0$.

Our findings have implications for similar tectonic settings such as the Chile and Alaska subduction zones that have experienced large and heterogeneous megathrust ruptures. For instance, one can show that the focusing of tsunami energy—caused by coastal curvature—is not expected in Chile (see Supporting Information). The bathymetry in these regions is also similar to Cascadia with almost uniform bathymetric

slopes and large-scale geometric coastal morphology, in contrast with regions of more complex bathymetry such as Japan. Similarly, by identifying the most hazardous segments of the subduction zone, our results can be used to assist in selecting sites for the new generation of DART tsunami sensors or novel technologies such as SMART cables (Howe et al., 2019). This is important for near-field tsunami warning because these instruments are mostly deployed on the up-dip side of trenches, where the identification of the main areas contributing to the tsunami hazard is crucial.

Data Availability Statement

All bathymetry data used in the main text or the supporting information are available via the General Bathymetric Chart of the Oceans (https://www.gebco.net/data_and_products/gridded_bathymetry_data/#global). The tsunami simulation code is maintained and distributed by the US National Oceanic and Atmospheric Administration (https://nctr.pmel.noaa.gov/nthmp/). Rupture data and tsunami simulation results are available via Deep Blue Data at https://doi.org/10.7302/xe96-3z26.

Acknowledgments
The manuscript significantly benefited from invaluable discussions with Jean-Paul Ampuero, Amanda Thomas, and Kelin Wang as well as the constructive comments from two anonymous reviewers. Some figures were drafted using the Generic Mapping Tools (Wessel & Smith, 1998). This study was supported by a National Science Foundation grant (PREEVENTS geosciences directorate No. 1663769).

References

Aki, K., & Richards, P. G. (2002). *Quantitative seismology*. University Science Books.
Atwater, B. F. (1987). Evidence for great Holocene earthquakes along the outer coast of Washington State. *Science*, *236*(4804), 942–944. https://doi.org/10.1126/science.236.4804.942
Atwater, B. F., Musumi-Rokkaku, S., Satake, K., Tsuji, Y., Ueda, K., & Yamaguchi, D. K. (2015). *The orphan tsunami of 1700: Japanese clues to a parent earthquake in North America*. University of Washington Press.
Atwater, B. F., Stuiver, M., & Yamaguchi, D. K. (1991). Radiocarbon test of earthquake magnitude at the cascadia subduction zone. *Nature*, *353*(6340), 156–158. https://doi.org/10.1038/353156a0
Ben-Menahem, A., & Rosenman, M. (1972). Amplitude patterns of tsunami waves from submarine earthquakes. *Journal of Geophysical Research*, *77*(17), 3097–3128. https://doi.org/10.1029/jb077i017p03097
Berger, M. J., George, D. L., LeVeque, R. J., & Mandli, K. T. (2011). The GeoClaw software for depth-averaged flows with adaptive refinement. *Advances in Water Resources*, *34*(9), 1195–1206. https://doi.org/10.1016/j.advwatres.2011.02.016
Courant, R., Friedrichs, K., & Lewy, H. (1928). Uber die partiellen differenzengleichungen der mathematischen Physik. *Mathematische Annalen*, *100*(1), 32–74. https://doi.org/10.1007/bf01448839
Crosson, R. S., & Owens, T. J. (1987). Slab geometry of the Cascadia subduction zone beneath Washington from earthquake hypocenters and teleseismic converted waves. *Geophysical Research Letters*, *14*(8), 824–827. https://doi.org/10.1029/gl014i008p00824
Darienzo, M. E., & Peterson, C. D. (1995). Magnitude and frequency of subduction-zone earthquakes along the northern Oregon coast in the past 3,000 years. *Oregon Geology*, *57*(1), 3–12.
Davies, G., Griffin, J., Løvholt, F., Glimsdal, S., Harbitz, C., Thio, H. K., et al. (2018). A global probabilistic tsunami hazard assessment from earthquake sources. *Geological Society, London, Special Publications*, *456*(1), 219–244. https://doi.org/10.1144/sp456.5
Geller, R. J. (1976). Scaling relations for earthquake source parameters and magnitudes. *Bulletin of the Seismological Society of America*, *66*(5), 1501–1523.
Goldfinger, C., Galer, S., Beeson, J., Hamilton, T., Black, B., Romsos, C., et al. (2017). The importance of site selection, sediment supply, and hydrodynamics: A case study of submarine paleoseismology on the Northern Cascadia margin. *Marine Geology*, *384*, 4–46. https://doi.org/10.1016/j.margeo.2016.06.008
Goldfinger, C., Nelson, C. H., Morey, A. E., Johnson, J. E., Patton, J. R., Karabanov, E. B., et al. (2012). Turbidite event history–methods and implications for Holocene paleoseismicity of the Cascadia subduction zone (Tech. rep.). *US Geological Survey*.
González, F. I., Geist, E. L., Jaffe, B., Kânoğlu, U., Mofjeld, H., Synolakis, C. E., et al. (2009). Probabilistic tsunami hazard assessment at seaside, Oregon, for near-and far-field seismic sources. *Journal of Geophysical Research*, *114*(C11), C11023. https://doi.org/10.1029/2008jc005132
González, F. I., LeVeque, R. J., Chamberlain, P., Hirai, B., Varkovitzky, J., & George, D. L. (2011). Validation of the geoclaw model. In *NTHMP MMS tsunami inundation model validation workshop*. GeoClaw Tsunami Modeling Group.
Green, G. (1838). On the motion of waves in a variable canal of small depth and width. *Transactions of the Cambridge Philosophical Society*, *6*, 457.
Griggs, G. B., & Kulm, L. (1970). Sedimentation in Cascadia deep-sea channel. *Geological Society of America Bulletin*, *81*(5), 1361–1384. https://doi.org/10.1130/0016-7606(1970)81[1361:sicdc]2.0.co;2
Heaton, T. H., & Snavely, P. D. Jr. (1985). Possible tsunami along the northwestern coast of the United States inferred from Indian traditions. *Bulletin of the Seismological Society of America*, *75*(5), 1455–1460. https://doi.org/10.1785/bssa0750051455
Howe, B. M., Arbic, B. K., Aucan, J., Barnes, C. R., Bayliff, N., Becker, N., et al. (2019). SMART cables for observing the global ocean: Science and implementation. *Frontiers in Marine Science*, *6*, 424. https://doi.org/10.3389/fmars.2019.00424
Kânoğlu, U., & Synolakis, C. E. (1998). Long wave runup on piecewise linear topographies. *Journal of Fluid Mechanics*, *374*, 1–28.
Kelsey, H. M., Nelson, A. R., Hemphill-Haley, E., & Witter, R. C. (2005). Tsunami history of an Oregon coastal lake reveals a 4600 yr record of great earthquakes on the Cascadia subduction zone. *Geological Society of America Bulletin*, *117*(7–8), 1009–1032. https://doi.org/10.1130/b25452.1
Li, S., Wang, K., Wang, Y., Jiang, Y., & Dosso, S. E. (2018). Geodetically inferred locking state of the Cascadia megathrust based on a viscoelastic Earth model. *Journal of Geophysical Research: Solid Earth*, *123*(9), 8056–8072. https://doi.org/10.1029/2018jb015620
Lindell, M. K., & Prater, C. S. (2010). Tsunami preparedness on the Oregon and Washington coast: Recommendations for research. *Natural Hazards Review*, *11*(2), 69–81. https://doi.org/10.1061/(asce)1527-6988(2010)11:2(69)
Mansinha, L., & Smylie, D. (1971). The displacement fields of inclined faults. *Bulletin of the Seismological Society of America*, *61*(5), 1433–1440.

Melgar, D. (2021). Was the January 26th, 1700 Cascadia earthquake part of an event sequence? *Journal of Geophysical Research*. Retrieved from https://eartharxiv.org/repository/view/2029/

Melgar, D., LeVeque, R. J., Dreger, D. S., & Allen, R. M. (2016). Kinematic rupture scenarios and synthetic displacement data: An example application to the Cascadia subduction zone. *Journal of Geophysical Research: Solid Earth*, *121*(9), 6658–6674. https://doi.org/10.1002/2016jb013314

Munk, W., Snodgrass, F., & Carrier, G. (1956). Edge waves on the continental shelf. *Science*, *123*(3187), 127–132. https://doi.org/10.1126/science.123.3187.127

Okal, E. A. (1988). Seismic parameters controlling far-field tsunami amplitudes: A review. *Natural Hazards*, *1*(1), 67–96. https://doi.org/10.1007/bf00168222

Park, H., Cox, D. T., Alam, M. S., & Barbosa, A. R. (2017). Probabilistic seismic and tsunami hazard analysis conditioned on a megathrust rupture of the Cascadia subduction zone. *Frontiers in built environment*, *3*, 32. https://doi.org/10.3389/fbuil.2017.00032

Peters, R., Jaffe, B., Gelfenbaum, G., & Peterson, C. (2003). Cascadia tsunami deposit database. In *US geological survey open-file report* (pp. 03–13). Retrieved from http://pubs.usgs.gov/of/2003/0013/

Plafker, G. (1997). Catastrophic tsunami generated by submarine slides and back-arc thrusting during the 1992 earthquake on eastern Flores I., Indonesia. *Geological Society of America Bulletin*, *29*(57).

Priest, G. R., Goldfinger, C., Wang, K., Witter, R. C., Zhang, Y., & Baptista, A. M. (2010). Confidence levels for tsunami-inundation limits in northern Oregon inferred from a 10,000-year history of great earthquakes at the Cascadia subduction zone. *Natural Hazards*, *54*(1), 27–73. https://doi.org/10.1007/s11069-009-9453-5

Priest, G. R., Witter, R. C., Zhang, Y. J., Wang, K., Goldfinger, C., Stimely, L. L., et al. (2013). *Tsunami inundation scenarios for Oregon* (Open-File Report O-13-19). Oregon Department of Geology Mineral Industries.

Rabinovich, A. B. (1997). Spectral analysis of tsunami waves: Separation of source and topography effects. *Journal of Geophysical Research*, *102*(C6), 12663–12676. https://doi.org/10.1029/97jc00479

Ramos, M. D., Huang, Y., Ulrich, T., Li, D., Gabriel, A. A., & Thomas, A. M. (2021). Assessing margin-wide rupture behaviors along the Cascadia megathrust with 3-D dynamic rupture simulations. *Journal of Geophysical Research: Solid Earth*, *126*, e2021JB022005. https://doi.org/10.1029/2021jb022005

Salaree, A., & Okal, E. A. (2020). Effects of bathymetry complexity on tsunami propagation: A spherical harmonics approach. *Geophysical Journal International*, *223*(1), 632–647. https://doi.org/10.1093/gji/ggaa334

Satake, K. (2015). Geological and historical evidence of irregular recurrent earthquakes in Japan. *Philosophical Transactions of the Royal Society A: Mathematical, Physical and Engineering Sciences*, *373*, 20140375. https://doi.org/10.1098/rsta.2014.0375

Satake, K., Shimazaki, K., Tsuji, Y., & Ueda, K. (1996). Time and size of a giant earthquake in Cascadia inferred from Japanese tsunami records of January 1700. *Nature*, *379*(6562), 246. https://doi.org/10.1038/379246a0

Satake, K., Wang, K., & Atwater, B. F. (2003). Fault slip and seismic moment of the 1700 Cascadia earthquake inferred from Japanese tsunami descriptions. *Journal of Geophysical Research*, *108*, 17. https://doi.org/10.1029/2003jb002521

Schmalzle, G. M., McCaffrey, R., & Creager, K. C. (2014). Central Cascadia subduction zone creep. *Geochemistry, Geophysics, Geosystems*, *15*(4), 1515–1532. https://doi.org/10.1002/2013gc005172

Shuto, N., Suzuki, T., & Hasegawa, K. (1986). A study of numerical techniques on the tsunami propagation and run-up. *Science of Tsunami Hazards*, *4*, 111–124.

Small, D. T., & Melgar, D. (2020). Geodetic coupling models as constraints on stochastic earthquake ruptures: An example application to PTHA in Cascadia. *Journal of Geophysical Research: Solid Earth*, *126*, e2020JB021149. https://doi.org/10.1029/2020JB021149

Stein, S., & Stein, J. (2014). *Playing against nature: Integrating science and economics to mitigate natural hazards in an uncertain world*. John Wiley and Sons.

Stein, S., & Wysession, M. (2009). *An introduction to seismology, earthquakes, and earth structure*. John Wiley and Sons.

Synolakis, C. E., Bernard, E. N., Titov, V. V., Kânoğlu, U., & González, F. I. (2008). Validation and verification of tsunami numerical models. In *Tsunami science four years after the 2004 Indian ocean tsunami* (pp. 2197–2228). Birkhäuser Basel. https://doi.org/10.1007/978-3-0346-0057-6_11

Thingbaijam, K. K. S., Martin Mai, P., & Goda, K. (2017). New empirical earthquake source-scaling laws. *Bulletin of the Seismological Society of America*, *107*(5), 2225–2246. https://doi.org/10.1785/0120170017

Thio, H. K., & Somerville, P. (2009). A probabilistic tsunami hazard analysis of California. In *TCLEE 2009: Lifeline earthquake engineering in a multihazard environment* (pp. 1–12). https://doi.org/10.1061/41050(357)57

Thio, H. K., Somerville, P., & Polet, J. (2010). Probabilistic tsunami hazard in California. In *Pacific earthquake engineering research center report*. UC Berkeley Publications.

Titov, V., Kânoğlu, U., & Synolakis, C. (2016). Development of MOST for real-time tsunami forecasting. *Journal of Waterway, Port, Coastal, and Ocean Engineering*, *142*, 03116004–1–03116004–16. https://doi.org/10.1061/(asce)ww.1943-5460.0000357

Titov, V. V., & Synolakis, C. E. (1998). Numerical modeling of tidal wave runup. *Journal of Waterway, Port, Coastal, and Ocean Engineering*, *124*(4), 157–171. https://doi.org/10.1061/(asce)0733-950x(1998)124:4(157)

Wang, K., & Tréhu, A. M. (2016). Invited review paper: Some outstanding issues in the study of great megathrust earthquakes – The Cascadia example. *Journal of Geodynamics*, *98*, 1–18. https://doi.org/10.1016/j.jog.2016.03.010

Watt, J. T., & Brothers, D. S. (2021). Systematic characterization of morphotectonic variability along the Cascadia convergent margin: Implications for shallow megathrust behavior and tsunami hazards. *Geosphere*, *17*(1), 95–117. https://doi.org/10.1130/ges02178.1

Wessel, P., & Smith, W. H. (1998). New, improved version of generic mapping tools released. *Eos, Transactions American Geophysical Union*, *79*(47), 579–579. https://doi.org/10.1029/98EO00426

Williamson, A., Melgar, D., & Rim, D. (2019). The effect of earthquake kinematics on tsunami propagation. *Journal of Geophysical Research: Solid Earth*, *124*, 11639–11650. https://doi.org/10.1029/2019jb017522

Witter, R. C., Zhang, Y., Wang, K., Priest, G. R., Goldfinger, C., Stimely, L. L., et al. (2011). Simulating tsunami inundation at Bandon, Coos County, Oregon, using hypothetical Cascadia and Alaska earthquake scenarios. In Oregon department of geology and mineral industries special paper (Vol. 43, pp. 57). State Library of Oregon.